

# Investigating the depolarization property of skin tissue by degree of polarization uniformity contrast using polarization-sensitive optical coherence tomography

**XIN ZHOU,<sup>1</sup> SINA MALOUFI,<sup>2</sup> DANIEL C. LOUIE,<sup>2,3,4</sup> NING ZHANG,<sup>1</sup> QIHAO LIU,<sup>1</sup> TIM K. LEE,<sup>2,3,4</sup> AND SHUO TANG<sup>1,2,\*</sup>**

<sup>1</sup>*Department of Electrical and Computer Engineering, University of British Columbia, Vancouver, BC V6T 1Z4, Canada*

<sup>2</sup>*School of Biomedical Engineering, University of British Columbia, Vancouver, BC V6T 1Z4, Canada*

<sup>3</sup>*Department of Dermatology and Skin Science, Photomedicine Institute, University of British Columbia, and Vancouver Coastal Health Research Institute, Vancouver, BC, V5Z 4E8, Canada*

<sup>4</sup>*Cancer Control Research Program, BC Cancer, Vancouver, BC, V5Z 1L3, Canada*

\*[tang@ece.ubc.ca](mailto:tang@ece.ubc.ca)

**Abstract:** The depolarization property of skin has been found to be important for skin cancer detection. Previous techniques based on light polarization lack the capability of depth differentiation. Polarization-sensitive optical coherence tomography (PS-OCT) has the advantage of both depth-resolved 3D imaging and high sensitivity to polarization. In this study, we investigate the depolarization property of skin tissue using PS-OCT, especially with the degree of polarization uniformity (DOPU) contrast. Well designed skin phantoms with various surface roughness levels and optical properties mimicking skin are imaged by PS-OCT and the DOPU values are quantified. The result shows a correlation between DOPU and surface roughness, where a higher roughness corresponds to a lower DOPU value. An index matching experiment with a water layer confirms the impact of surface condition on light depolarization. Refraction of backscattered photons on the surface boundary is attributed to the broadening of backscattering angle and thus depolarization. To the best of our knowledge, this is the first time the impact of surface roughness on DOPU is reported and its mechanism explained. Furthermore, through preliminary *in vivo* skin imaging, the capability of DOPU in detecting depolarization in skin is demonstrated. By utilizing the 3D imaging from PS-OCT, DOPU can offer a high-resolution depth differentiation and quantification of depolarization in skin tissue.

© 2021 Optical Society of America under the terms of the [OSA Open Access Publishing Agreement](#)

## 1. Introduction

Skin cancer is one of the most prevalent forms of cancer in the western world. Its incidence rate, treatment costs, and associated health burdens have been steadily increasing [1–2]. The major types of skin cancer include basal cell carcinoma (BCC), squamous cell carcinoma (SCC), and melanoma. BCC and SCC are also grouped together as non-melanoma skin cancers. Despite making up approximately 1% of skin cancer cases, melanoma is responsible for a disproportionate majority of skin cancer deaths [2]. Five-year survival rates for melanoma can be as high as 99% when detected early, but fall to 65% if the disease reaches the lymph nodes, and 25% after metastasis to distant organs – underscoring the importance of early detection [3]. Unfortunately, diagnosis of melanoma is often difficult because it visually resembles benign skin lesions such as seborrheic keratosis (SK) [4]. The current gold standard for diagnosis is a biopsy, but it is an invasive and uncomfortable procedure. One study showed that over 80% of biopsies ordered by primary care providers were found to be benign, meaning that biopsies are often performed when there is no cancer present [5]. Given this, developing a non-invasive and accurate tool for

skin cancer detection is a topic of great interest. General visual indicators of melanoma include changes in size, elevation, and color; irregular borders can also be a possible sign to differentiate melanoma from benign lesions [6,7]. However, these features are generally qualitative and are not always conclusive, making diagnosis difficult. In the cases where cancerous growths and benign lesions are not readily distinguishable based on visual features, research has shown that structural features such as tissue surface roughness can help differentiate growths that otherwise appear similar [8]. A micro-topographical skin study has shown that both BCC and melanoma samples examined had significantly different surface roughness values compared to healthy skin and benign lesions [9]. However, as the surface roughness of a patient's skin can be affected by factors such as age, sex, and lifestyle, more studies in this area are necessary for a conclusive correlation.

Light polarization techniques have been widely applied toward skin assessment, where polarized light is shined on tissue and the polarization state of backscattered light is analyzed [10]. Traditional polarization techniques involve rotating a linear polarizer in front of a detector to sequentially detect the intensities in the parallel- and cross-polarization states, respectively [11–15]. Jacques et al. [15] used a camera to record the backscattered light in the two polarization states and then calculated a depolarization ratio image by subtracting their intensities. They showed that the depolarization ratio image enhanced the contrast between healthy skin and lesions. Nevertheless, the sequential acquisition was sensitive to temporal fluctuations such as light source instability and motion artifacts. Tchvialeva et al. [16] improved this approach by recording the parallel- and cross-polarization signals simultaneously using two detection channels. They obtained the speckle difference image from the two simultaneously acquired speckle images without the influence of temporal fluctuations. By analyzing the spatial distribution of the depolarization ratio in the speckle difference image, it performed well in differentiating benign lesions from various cancerous lesions. However, they still had difficulty in differentiating melanoma from benign nevus.

Another polarization-based technique is Stokes polarimetry, where a full Stokes vector can be measured by varying the input light polarization and analyzing the corresponding output polarization [17,18]. Degree of polarization (DOP) is calculated from the Stokes vector, which quantifies the percentage of the polarized light intensity over the total intensity. Louie et al. [17] developed a Stokes polarimetry probe using both linear and circularly polarized incident light, and four photodetectors equipped with film polarizing filters. They found that higher surface roughness was associated with a lower DOP. In their study, melanoma, which showed a higher DOP than benign nevus, was successfully differentiated from all other types of skin lesions studied, but their sample size (5 melanoma) was small for a statistical investigation. Ghassemi et al. developed a Stokes imaging polarimetry that captured Stokes vector images at 16 different azimuth illumination angles by sequential measurements [18]. They quantified the dependence of DOP and the principle angles of polarization ellipses on the illumination angle and preliminarily demonstrated an ability to differentiate melanoma from benign lesions. They reported that melanoma has a lower DOP compared to benign nevus, which is opposite from the findings in Ref. [17]. The contradictory findings in those studies is possibly due to their different approaches and the different stages of melanoma being observed [6,19]. Other than surface roughness, melanosomes have also been found to depolarize light due to their non-spherical shape. A high concentration of melanin in the retinal pigment epithelium (RPE) layer has been reported to cause polarization scrambling in retinal imaging [20]. Thus, a high concentration of melanin could also affect DOP in skin lesions. While the above polarization techniques show promise, a major limitation is the lack of depth resolution, where they cannot differentiate the backscattered signals coming from the tissue surface versus that from the sub-surface layers (e.g. locally concentrated pigments).

Optical coherence tomography (OCT) is a non-invasive 3D imaging modality that can offer volumetric information with a high spatial resolution (3–15  $\mu\text{m}$ ) and penetration up to 1.5 mm [21,22]. OCT has great clinical success as an ophthalmic diagnostic tool, while it has also attracted attention for its potential in skin imaging, providing both surface profile and volumetric depth-resolved tissue information simultaneously [23]. Due to its ability to assess the 3D morphology of tissues, conventional OCT has assisted physicians in detecting BCCs. Cross-sectional OCT images have been assessed qualitatively for indicators of skin cancer such as protrusions into the dermis, rupturing of the dermo-epidermal junction, and cyst-like structures in the dermis [24]. However, as conventional OCT only utilizes the intensity of backscattered signals, it has encountered difficulty in detecting melanoma [25].

Polarization-sensitive OCT (PS-OCT) is a functional extension of OCT that can simultaneously provide multiple contrasts such as phase retardation, optic axis, and degree of polarization uniformity (DOPU), in addition to conventional intensity signal [26]. Phase retardation and optic axis contrasts are related to the tissue birefringence properties, which are sensitive to the collagen organization in skin. DOPU contrast can quantify polarization scrambling within small, selected volumes, and a higher DOPU value usually correlates with a higher DOP [27]. In PS-OCT imaging, DOPU contrast is depth-resolved and can generate 3D images that represent the depolarization effects from different locations and structures in a sample. Considering the enhanced sensitivity offered by polarization properties, imaging skin with PS-OCT has garnered attention [28–32]. Many early investigations of skin imaging by PS-OCT were mainly focused on phase retardation and optic axis contrasts, which studied the collagen organization in skin [28–30]. Following this, further attention has been spent on BCC detection, in which collagen degeneration can be assessed by a reduction in tissue birefringence [33]. Duan et al. developed an automated classifier using features from the scattering intensity and birefringence (usually lower in tumours due to collagen disruptions) measured by PS-OCT to detect *ex-vivo* BCC with a sensitivity and specificity of over 90% [34]. The same group expanded their work to a clinical setting and reported sensitivity and specificity values of over 95% [35]. However, their methods mainly focused on birefringence properties, which could be similar between melanoma and other non-melanoma lesions. When imaging thick skin, random optic axis and phase retardation were observed in stratum corneum (SC), the first layer in epidermis [30]. Such random polarization properties were further assessed by the DOPU images, where a depolarizing band with low DOPU was observed in the same region [31–32]. This was explained as the inhomogeneity in SC [31]. To the best of our knowledge, few studies have applied PS-OCT toward melanoma detection, and especially the potential of DOPU for characterizing the depolarization properties of tissue has not been fully utilized.

We propose to assess polarization and depolarization properties of skin tissue using PS-OCT, especially with the DOPU contrast. PS-OCT combines the advantages of volumetric imaging capabilities of OCT with the contrast provided by polarization measurements. As a depth-resolved imaging, the DOPU contrast from PS-OCT has the potential to differentiate depolarization from different regions. In this study, well designed skin phantoms with various surface roughness levels and optical properties resembling skin will be studied by DOPU. The impact of surface roughness on DOPU will be analyzed and quantified in details. Human skins with different superficial conditions are also imaged to demonstrate the clinical potential of DOPU in skin assessment.

## 2. Materials and methods

### 2.1. Sample preparation

Four rough skin phantoms with different bulk optical properties (labelled as P1 to P4) were constructed as per a previously published recipe [36]. On each phantom, seven different regions with controlled surface roughness levels (labelled as R1 to R7) were constructed by curing the

resin mixture over a metal roughness comparator (Microsurf #334 comparator, Rubert & Co Ltd., Cheadle, United Kingdom). The roughness levels were validated by an optical profilometer (Wyko NT2000, Veeco, Tucson, Arizona) with an axial resolution of 0.05  $\mu\text{m}$ , lateral resolution of 0.5  $\mu\text{m}$ , and standard error of 10%. The fabricated root mean square (RMS) roughness levels of the phantoms are 1.1, 2.2, 4.5, 9, 18, 34, and 68  $\mu\text{m}$  for R1 to R7, respectively. Table 1 lists the absorption and reduced scattering coefficients [17,36].

**Table 1. Bulk optical properties of the rough skin phantoms**

	Absorption coefficient $\mu_a$ ( $\text{mm}^{-1}$ )	Reduced scattering coefficient $\mu'_s$ ( $\text{mm}^{-1}$ )
Phantom P1	$0.28 \pm 0.02$	$0.50 \pm 0.01$
Phantom P2	$0.09 \pm 0.02$	$1.29 \pm 0.05$
Phantom P3	$0.17 \pm 0.02$	$0.78 \pm 0.14$
Phantom P4	$0.09 \pm 0.02$	$0.55 \pm 0.02$

## 2.2. PS-OCT imaging and DOPU contrast

All images were acquired by a custom-built Jones-matrix-based PS-OCT system previously described in Ref. [37]. The system uses a swept-wavelength laser source (Axsun Technology Inc., MA), with a center wavelength of 1.06  $\mu\text{m}$ , full-width-at-half-maximum (FWHM) bandwidth of 111 nm, and scanning width of 123 nm. The sweeping rate of the light source is 100 kHz and the average output power is 30 mW. The sensitivity of the PS-OCT system is 92 dB. The lateral resolution is  $\sim 19.2 \mu\text{m}$  and the axial resolution is  $\sim 8.1 \mu\text{m}$  in air. In B-scan image, each pixel is  $\sim 9.7 \mu\text{m} \times 3.6 \mu\text{m}$  (in tissue) in horizontal  $\times$  axial directions, respectively. Using the PS-OCT system, co-registered OCT intensity image and DOPU image are acquired simultaneously from 3D volumetric scans. Each volume is recorded in 10 seconds.

The Stokes vector  $\mathbf{S}$  is calculated from the complex OCT output signals obtained from a polarization detection unit,  $\mathbf{E}_A(z)$  and  $\mathbf{E}_B(z)$ , which correspond to the signals in the parallel and perpendicular polarizations, respectively.

$$\mathbf{S} = \begin{bmatrix} I \\ Q \\ U \\ V \end{bmatrix} = \begin{bmatrix} |\mathbf{E}_A(z)|^2 + |\mathbf{E}_B(z)|^2 \\ |\mathbf{E}_A(z)|^2 - |\mathbf{E}_B(z)|^2 \\ \mathbf{E}_A(z)\mathbf{E}_B(z)^* + \mathbf{E}_A(z)^*\mathbf{E}_B(z) \\ i\left(\mathbf{E}_A(z)\mathbf{E}_B(z)^* - \mathbf{E}_A(z)^*\mathbf{E}_B(z)\right) \end{bmatrix} \quad (1)$$

As OCT is a coherent technique, DOPU detects depolarization by quantifying the spatial fluctuation of the Stokes vector [26–27]. With the capability of detecting the polarization scrambling caused by melanin, DOPU was originally applied toward selective visualization of the RPE layer in the retina. DOPU is defined based on the Stokes parameters as:

$$DOPU = \sqrt{\bar{Q}^2 + \bar{U}^2 + \bar{V}^2} \quad (2)$$

where  $(\bar{Q}, \bar{U}, \bar{V}) = \left(\frac{1}{N} \sum_i \frac{Q_i}{I_i}, \frac{1}{N} \sum_i \frac{U_i}{I_i}, \frac{1}{N} \sum_i \frac{V_i}{I_i}\right)$  and  $i$  indicates the  $i$ -th pixel within a spatial kernel of  $N$  pixels by which DOPU is defined. Since OCT is based on a coherent detection mechanism, the light detected from a single speckle is always fully polarized. However, for the scattered signals from a depolarizing medium, the polarization states may vary spatially, where the complex signals from adjacent speckles are usually random, or mathematically uncorrelated. DOPU is a quantification for such spatial variations of polarization states. In our study, a kernel

size of 3 pixels (horizontal)  $\times$  2 pixels (axial) that corresponds to  $29\ \mu\text{m} \times 7\ \mu\text{m}$  is applied. DOPU values range from 0 to 1. A DOPU of 1 means that the polarization states among the neighbouring pixels are uniform, indicating that there is no polarization scrambling. When the DOPU value is close to 0, there are significant spatial fluctuations in the polarization states of the backscattered light among neighbouring pixels, indicating high polarization scrambling and thus depolarization from that area of tissue.

### 2.3. Depth-resolved DOPU imaging and impact of surface roughness

OCT is an interference technique that detects backscattered light within the coherence length of the light source. Therefore, the DOPU imaging in PS-OCT is depth-resolved which can detect depolarization from different locations. In tissue, multiple mechanisms can cause depolarization [10]. Scattering from non-spherical particles causes depolarization because the parallel and perpendicular polarizations have different scattering efficiencies [38]. A rough surface can cause depolarization due to reflection and refraction on the boundary [17,39–40]. Based on the 3D imaging capability of DOPU, it is possible to separate where the scattering and depolarization is coming from.

Figure 1 illustrates the principle of signal detection in DOPU from a layered tissue structure. Figure 1(a) shows a DOPU image of retina where the RPE layer shows low DOPU (yellow band). Figures 1(b) and 1(c) show the detection of backscattered light through a flat and a rough surface, respectively. Figure 1(d) illustrates the pattern of scattering efficiency for parallel and perpendicular polarizations from a small spherical particle in the Rayleigh scattering regime [10]. For non-spherical particle or Mie scattering, the pattern of the scattering efficiency is more complex and non-isotropic [10].

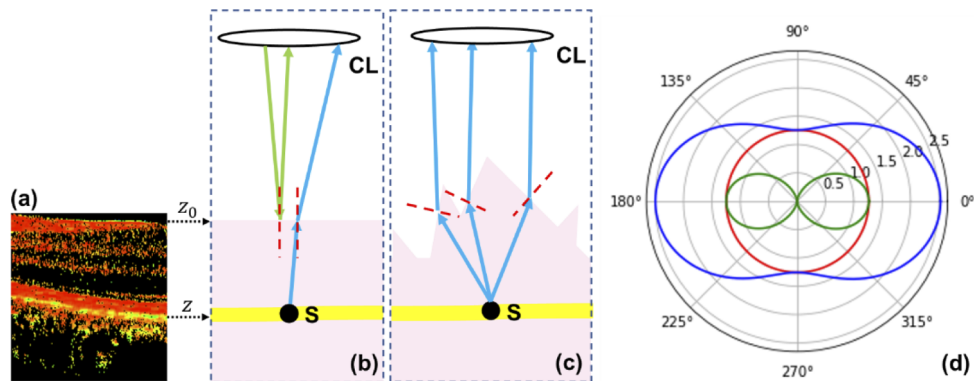


**Fig. 1.** Principle of signal detection in DOPU from tissue. (a) DOPU image of retina. (b) and (c) detection of backscattered light through a flat and a rough surface, respectively. (d) The scattering efficiency polar plot for perpendicular (red) and parallel (green) polarizations and unpolarized (blue) incident light from a small spherical particle. S: scatter; CL: collecting lens.

When light shines on tissue, some light gets reflected back by the tissue surface (as shown by the green arrows in Fig. 1(b) at depth  $z_0$ ). The reflected signal is detected and shown at the tissue surface on the DOPU image. If any depolarization is caused by surface reflection, it would be shown as low DOPU signals at the surface. After light entering the tissue, some light can be scattered back by particles inside the tissue (e.g. the scatter S at depth  $z$ ). The depth location of the scatter S is resolved and obtained by the coherence gating of the PS-OCT. Whether the polarization of the scattered light is maintained or changed from the incident light depends on the shape and size of the particle and the scattering angle. As shown in Fig. 1(d),



for any scattering angle, except  $\theta = 0^\circ$  and  $180^\circ$ , the scattering efficiencies are different for light in the parallel and perpendicular polarizations respectively, with more preferable intensity in the perpendicular polarization to the scattering plane. Such difference further increases as the scattering angle approaches  $\theta = 90^\circ$  or  $270^\circ$ . For non-spherical particles, the pattern of scattering efficiency becomes more complex and more significant depolarization can occur than for spherical particles. In DOPU image, the depolarization caused by non-spherical particles are located and differentiated in specific layers or regions, such as the RPE layer in retina (located at depth  $z$  in Fig. 1(a)).

Furthermore, when the backscattered light returns back to the tissue surface boundary, refraction occurs which deviates the light direction based on the local normal of the surface. Only the light that falls inside the light cone of the collection lens can be detected by the system. For a relatively flat surface as shown in Fig. 1(b), OCT detects those photons that are scattered near the exact backscattering direction within a small light cone determined by the numerical aperture (NA) of the collection optics. The polarization states of the scattered photons are mostly maintained and  $\text{DOPU} \approx 1$  because the scattering angle  $\theta \approx 180^\circ$ . For a relatively rough surface as shown in Fig. 1(c), the rough surface can be regarded as an ensemble of many small sub-surfaces with randomly tilted angles. Those small sub-surfaces refract the backscattered photons to different directions and further broaden the range of the scattering angles of the photons that can be collected by the OCT system. For the photons that have been scattered at angles  $\theta \neq 180^\circ$ , change of the polarization from incident light occurs because the scattering efficiencies for the parallel and perpendicular polarizations are different. In this situation, the spatial fluctuation of the rough surface increases the randomness and broadens the range of the scattering angles captured by the OCT system, which results in higher randomness of polarization states and thus a lower DOPU. While the depolarization is originated by scattering, the rough surface enhances the detection of those photons that would normally not be detected in an exact-backscattering detection geometry. As refraction on the surface boundary occurs to all the backscattered photons coming from below the surface, the impact of surface roughness on DOPU should affect all the pixels below the surface. To quantify the effect of refraction by the surface on DOPU, a selected band below the tissue surface will be used as described in Section 2.4.

While OCT detects mostly single-scattered photons, multiple-scattered photons could also possibly be detected [42]. Multiple scattering is known to depolarize light after the photons have been scattered and changed directions for multiple times. Separating the single-scattered and multiple-scattered photons is a meaningful yet challenging question, and is out of the scope of the current work.

#### 2.4. Quantification analysis

From the PS-OCT system, both intensity and DOPU contrast images are obtained. In the intensity OCT images, strong reflections are normally observed at the tissue surface. These reflections may cause a glaring effect that disturbs the Jones Matrices measured at the surface boundary. Moreover, OCT signal intensity is attenuated as light penetrates deeper into tissue, causing a drop of signal-to-noise ratio (SNR) in the deep regions. Therefore, both the surface glaring and the attenuation of SNR in the deep regions can result in a reduced reliability in DOPU calculation. To obtain a consistent and reliable quantification of DOPU for the various tissue phantoms and roughness regions, a spatial band is selected below the surface. Since refraction on the surface boundary occurs to all the backscattered photons coming from below the surface, the DOPU quantification obtained from the band can still represent the impact from the surface roughness. A custom-built segmentation algorithm is first applied to detect the tissue surface based on information from the OCT data volume. Afterwards, a thin band with a height of 20 pixels is selected after excluding the first 3 pixels below the tissue surface. Within the selected band, the average DOPU is calculated, and a new quantity named partial scrambling ratio (PSR)

is defined as follows,

$$\text{PSR} = \frac{\text{Number of DOPU Pixels} \in (a_1, a_2)}{\text{Number of DOPU Pixels} \in (0, 1]} \quad (3)$$

Here, the pixel numbers are counted from the DOPU data volume within the selected band. In the numerator, only the pixels considered to exhibit “partial scrambling” are counted, which is defined as a DOPU value in the range  $(a_1, a_2)$ . In the denominator, the number of pixels with DOPU values in the range  $(0, 1]$  are counted for the purpose of normalization. Pixels with intensity SNR < 13 dB are set as background and assigned a value of DOPU = 0, where those pixels are excluded in the calculation of DOPU and PSR to reduce the influence of noise. PSR can quantify how a sample scrambles polarized incident light to partially polarized light. In this study,  $a_1$  and  $a_2$  were determined empirically to be 0.6 and 0.95, respectively. The pixels with DOPU < 0.6 are considered to be depolarized, and those with DOPU > 0.95 as polarization-maintaining. The pixels with DOPU values between 0.6 and 0.95 are considered to exhibit partial scrambling.

### 3. Results

#### 3.1. PS-OCT imaging of skin phantoms

PS-OCT imaging is applied on the four skin mimicking phantoms containing different surface roughness regions. Images of both the intensity and DOPU contrasts are obtained. The intensity contrast shows the morphology of the tissue phantom while the DOPU contrast has the capability in detecting light depolarization, which is affected by scattering inside tissue and surface conditions [41]. Figure 2 shows the PS-OCT imaging results from regions R1 to R7, respectively, of phantom P3. The left column shows the *en face* intensity projection image, the middle column shows a representative cross-sectional B-scan intensity image (grayscale) and DOPU image (colored), and the right column shows the DOPU histogram. Each histogram is generated from 4 repeat-measurement data volumes, where each volume contains 250 B-scans.

First, the *en face* intensity projection images show the tissue morphology in a top-down view. From region R1 to R7, granular patterns are observed, which gradually change from fine to more coarse patterns; large holes are also observed in R6 and R7, which indicate a high surface roughness. Second, from the B-scan intensity images, the surface profile of the tissue phantom can be observed, which is only limited by the resolution of the PS-OCT system. From R1 to R3, little change in the surface profile is observed because the roughness levels are below the system resolution. However, from R4 to R7, gradually increasing roughened surface profiles are observed. While the intensity OCT image can visualize the surface roughness directly, it is limited to roughness levels that are above its spatial resolution. In other words, intensity OCT images are not sensitive to micro-roughness features that are below the system resolution. Third, from the B-scan DOPU images, the increasing surface roughness from R1 to R7 is sensitively detected by an increasing number of pixels with lower DOPU values, indicated by the pixels colored by yellow to green. For example, in R1, the DOPU image shows almost no depolarization (DOPU = 1, all red color). In R2 and R3, the DOPU images clearly show a few yellow speckles (slightly lower DOPU values). More yellow to green speckles are shown in the DOPU images from R4 to R7, indicating a further decrease in DOPU. Finally, the DOPU histograms show a consistent trend of changes as the surface roughness increases. Each histogram distribution has been normalized to have a total area equal to one and thus can be viewed as a probability density function of the DOPU distribution. As roughness increases from R1 to R7, the peak of the DOPU distribution shifts towards the left (lower DOPU), and the distribution function becomes more broadened and skewed towards the left. In the histogram, the average and standard deviation of DOPU are also calculated, where the average DOPU is found to decrease consistently from R1 to R7. In the skin phantom, DOPU detects surface roughness with very high sensitivity, even for roughness levels below the spatial resolution.

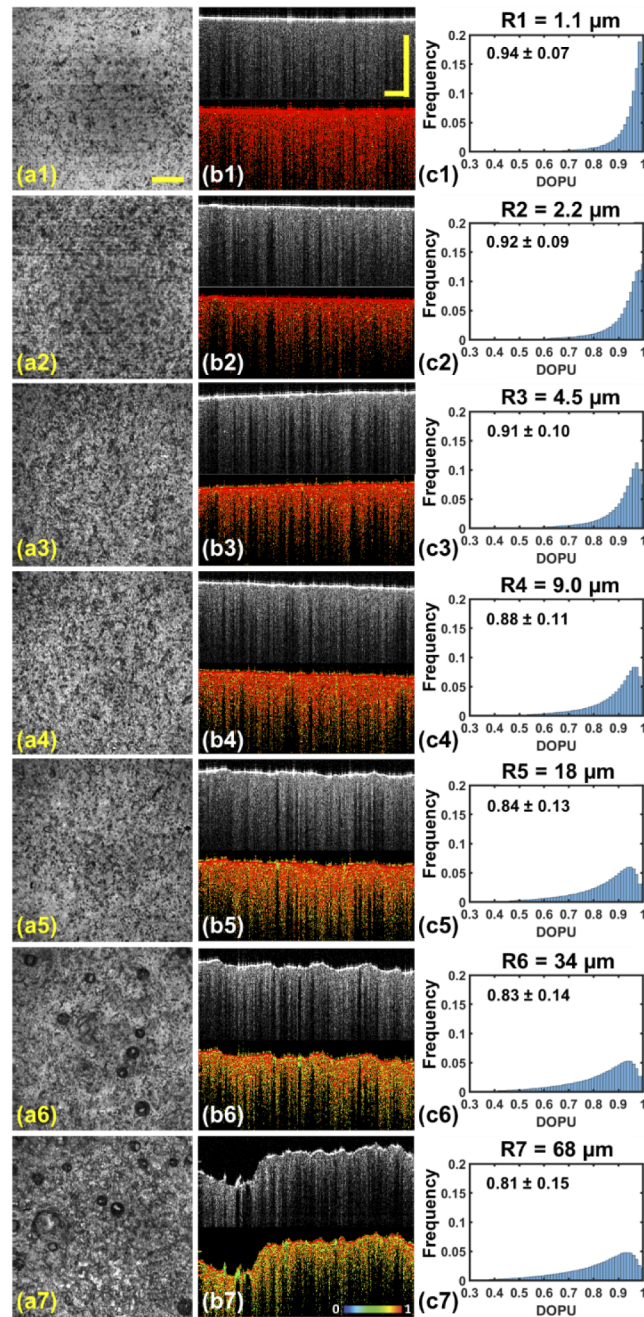


**Fig. 2.** PS-OCT imaging of different roughness regions from R1 to R7. Left column: *en face* intensity projection image; Middle column: B-scan intensity image (grayscale) and DOPU image (colored); Right column: DOPU histogram. The average and standard deviation of DOPU are also shown in each histogram. Scale bars are 500  $\mu\text{m}$ .



### 3.2. Quantification of surface roughness

Quantification of surface roughness has been reported using a morphological analysis based on OCT intensity signals [23]. This method evaluates surface roughness by calculating the difference between the surface profile and its corresponding fitted curve in a B-scan image. We also applied this method to the intensity images acquired by the PS-OCT system on regions R1 to R7 to calculate the RMS roughness, as shown in Fig. 3(a). From R4 to R7, the intensity-based method shows the correct roughness. However, for R1 to R3, the measurement plateaus at the resolution limit as those roughness levels are below the spatial resolution of the system.

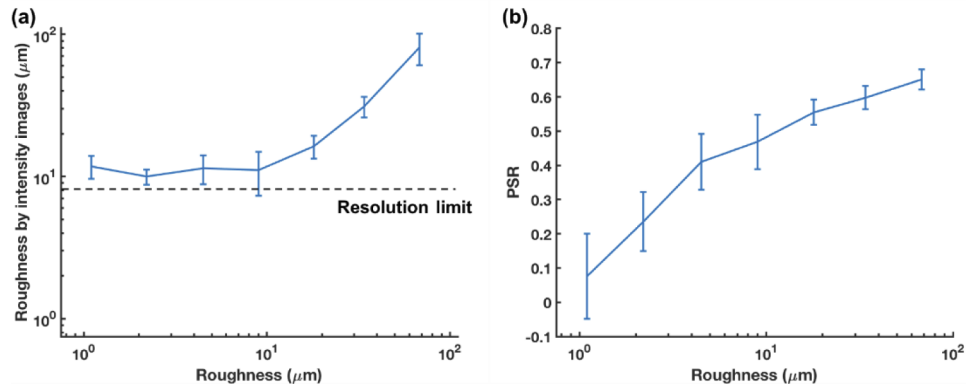


**Fig. 3.** Quantification of surface roughness. The X-axis shows the known, fabricated roughness values, and the Y-axis shows the roughness measured from intensity image (a), and PSR calculated from the DOPU image (b). The dashed line shows the resolution limit of the system. The known roughness values of R1 to R7 are 1.1, 2.2, 4.5, 9, 18, 34, and 68  $\mu\text{m}$ , respectively. Error bars show the standard deviation among different B-scans.

On the other hand, DOPU can differentiate surface roughness with high sensitivity even below the resolution limit. Figure 3(b) shows PSR for the roughness levels R1 to R7. PSR increases consistently as the roughness level increases from R1 to R7. It is shown that PSR can differentiate all the measured roughness levels in the skin phantom, especially for the micro-roughness ( $< 10 \mu\text{m}$ ) which cannot be detected by the intensity-based method.

### 3.3. Measurements from phantoms with various optical properties

The four phantoms P1, P2, P3, and P4, with different optical absorption and scattering coefficients, have been measured by PS-OCT. Figures 4(a) and 4(b) show the average DOPU and PSR, respectively, for the different roughness regions from R1 to R7. Each region is measured four separate times to ensure repeatability, and the error bars show the standard deviation among the four measurements. As the roughness level increases, a positive correlation in PSR and a negative correlation in DOPU are consistently observed for all four phantoms. This kind of correlation is consistent for all the phantoms even though they have different absorption and scattering coefficients.

To investigate the influence of the absorption and scattering coefficients on DOPU, the DOPU obtained from the same roughness regions (e.g. R1 or R4, as indicated by the arrows in Fig. 4(a)) are compared among the four phantoms. Figures 5(a) and 5(b) show the relationships between DOPU and absorption coefficient  $\mu_a$ , and reduced scattering coefficient  $\mu'_s$ , respectively. As we can see, lower DOPU is associated with a higher  $\mu'_s$  and lower  $\mu_a$ . The physical mechanism of this effect is not clear yet and we suspect that it is possibly related to multiple scattering. As  $\mu'_s$  increases, a medium with higher scattering will cause more multiple-scattered photons, which results in depolarization. As  $\mu_a$  decreases, more photons will be detected from deeper regions,

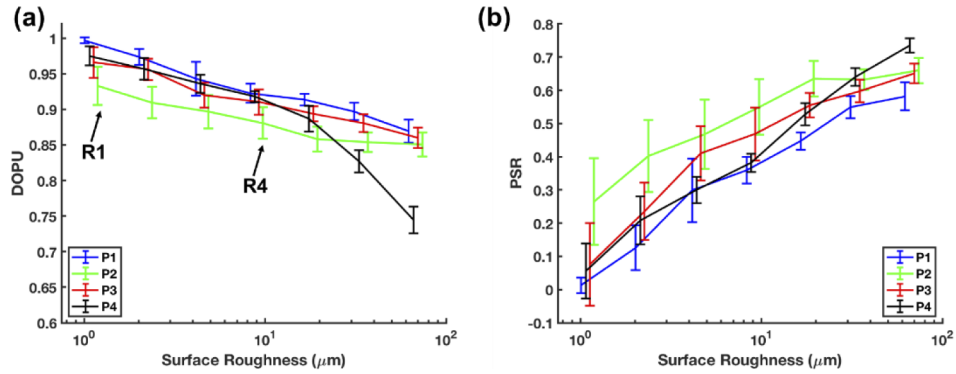


**Fig. 4.** Measured results of DOPU (a) and PSR (b) for the four phantoms. For each roughness level, the data points are slightly shifted horizontally for easier visibility. The roughness values of R1 to R7 are 1.1, 2.2, 4.5, 9, 18, 34, and 68  $\mu\text{m}$ , respectively. Error bars show the standard deviation among four repeated measurements.

which tend to have higher amounts of multiple scattering and depolarization. The situation becomes more complex when the effects of  $\mu'_s$  and  $\mu_a$  oppose each other, such as in phantom P4 where both  $\mu'_s$  and  $\mu_a$  are relatively low. In Fig. 5(a), while both P2 and P4 have low absorption coefficients, P4 shows a higher DOPU than P2 because P4 has a lower scattering coefficient.

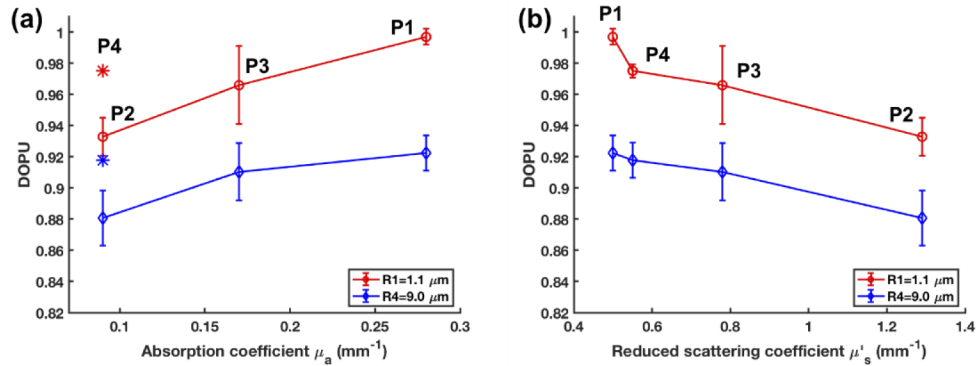


**Fig. 5.** (a) DOPU versus absorption coefficient  $\mu_a$  and (b) DOPU versus reduced scattering coefficient  $\mu'_s$ . The DOPU values are measured at the same roughness level at R1 = 1.1  $\mu\text{m}$  or R4 = 9.0  $\mu\text{m}$ , respectively.

### 3.4. Refractive index matching for reducing surface effects

To examine the impact of surface roughness on DOPU, experiments attempting to match the refractive index at the tissue surface were also carried out. The above-mentioned experiments were carried out with air as the medium above the tissue surface (i.e. no index matching). A layer of water was applied to the phantom P2 to reduce the surface effect through improved index matching. Figure 6 shows the intensity and DOPU images with (right) and without (left) an affixed layer of water. A piece of cover glass was used to hold the water layer in place. In the intensity B-scan image (Fig. 6(a)), the surface area shows very high backscattering intensity due to surface reflection. After applying a water layer, the surface reflection is significantly reduced

as shown in Fig. 6(b). Comparing the DOPU images in Figs. 6(c) and 6(d), a slight reduction of yellow speckles is observed when index matching is applied, especially from the surface area.

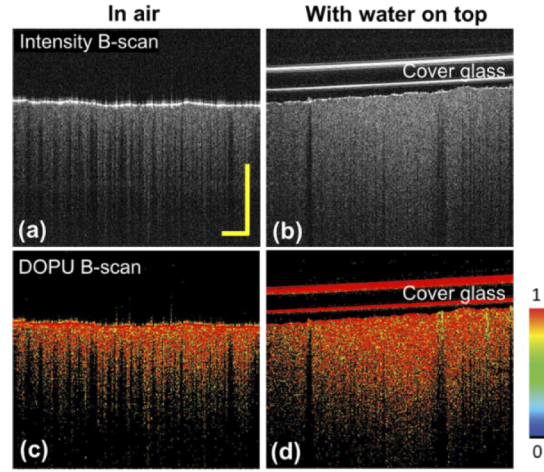


**Fig. 6.** Comparison of PS-OCT images without or with index matching, measured in air or with a water layer on top of the phantom, respectively. Intensity image (grayscale) and DOPU image (colored).

Figures 7(a) and 7(b) show the average DOPU and PSR, respectively, for the roughness regions from R1 to R7, with and without index matching. With index matching, the DOPU value is found to be higher than that without index matching, indicating reduced polarization scrambling. Similarly, a lower PSR is obtained with index matching compared to without index matching, which corresponds to lower polarization scrambling. By applying an index matching water layer, the surface effect is significantly reduced, which results in the reduction of the depolarization effect caused by irregular surface boundaries. This demonstrates that the DOPU features measured from within tissues are sensitive to surface conditions. Since the refractive index of water does not completely match with that of the tissue, the correlation between DOPU or PSR and the surface roughness are still observed, where a decreasing DOPU and increasing PSR are observed with increasing roughness.

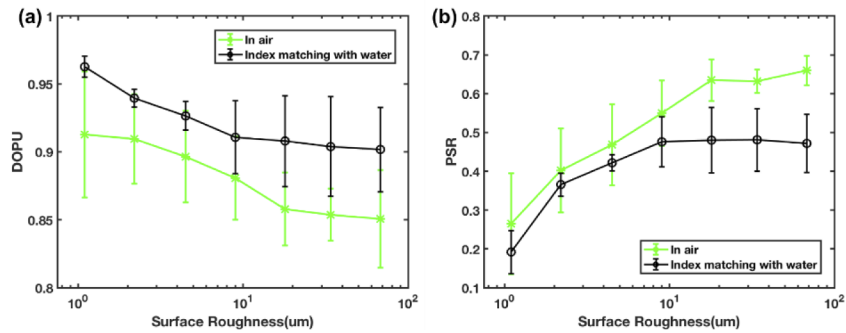


**Fig. 7.** Quantification of DOPU (a) and PSR (b) without or with index matching, measured in air or with a water layer on top of the phantom, respectively. The roughness values of R1 to R7 are 1.1, 2.2, 4.5, 9, 18, 34, and 68  $\mu\text{m}$ , respectively. Error bars show the standard deviation among four repeated measurements.

### 3.5. Skin imaging

To validate the capability of DOPU in skin assessment, preliminary *in vivo* skin imaging was carried out on two volunteers. The study has been approved by the University of British Columbia research ethical board under H19-02887 and informed consent has been obtained from the volunteers. Figure 8 shows the PS-OCT images measured from the ventral forearm of a male (first column), the ulnar palm edge of a female (second column), the ulnar palm edge of the same male (third column), and a healthy pigment mole on the arm of the same male (forth column). The *en face* intensity projection images are shown in the first row, the B-scan intensity images in the second row, and the DOPU images in the third row. The *en face* intensity projection image shows the top-down view of the skin morphology, where the ventral forearm shows a regular furrow pattern and the palm edge shows fewer furrows but more scale-like patterns. The B-scan intensity image shows the cross-sectional view of the skin, where multiple layers can be differentiated. In the palm edge, the stratum corneum (SC), stratum spinosum (SS), and dermis can be differentiated. In the ventral forearm, as the skin is much thinner [43], only the epidermis and dermis can be differentiated. In the DOPU image, a distinct yellow band is observed in the palm edges, similar findings were also reported by PS-OCT imaging on thick skin sites [31–32]. The lower DOPU value (yellow band) indicates that this layer of tissue tends to have high polarization scrambling. The thickness of the low DOPU band in the palm edge of the male and female volunteers is about 60  $\mu\text{m}$  and 20  $\mu\text{m}$ , respectively. The yellow band is not observed in the forearm, which is also consistent with literature [31]. Considering the anatomy and features of the skin layers, this highly depolarizing layer is likely the SC [31–32]. SC is the first layer of skin and is composed of multiple layers of flattened cells with no nuclei or cell organelles [44]. In the B-scan intensity image, the first low scattering layer corresponds to the SC where the lower scattering is mainly due to the cells containing no nuclei. Cell nucleus is a major structure for scattering light due to its high refractive index from condensed DNA. The next high scattering layer is likely the SS, which consists of more roundish cells that contain nuclei [44].

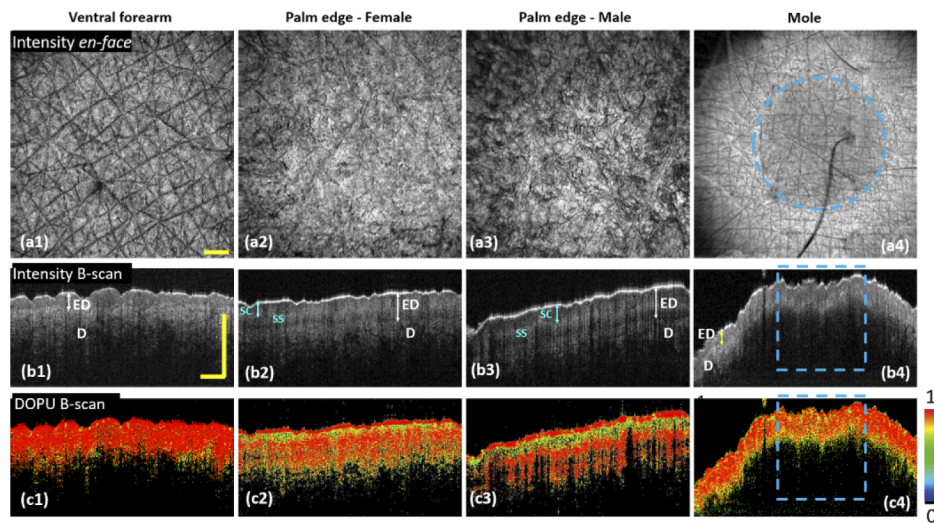


**Fig. 8.** PS-OCT imaging of human skin. (a) *En face* intensity projection image, (b) B-scan intensity image, and (c) B-scan DOPU image. From left to right are four cases measured from the ventral forearm, ulnar palm edge of a female, ulnar palm edge of a male, and a healthy pigment mole, respectively. ED: epidermis, D: dermis, SC: stratum corneum, SS: stratum spinosum. The mole region is marked by a dashed circle or box. Scale bars are 500  $\mu\text{m}$ .



The yellow band in the DOPU image matches with the low scattering layer in the intensity image. The flattened cells in the SC can be considered as non-spherical scattering particles, which can depolarize light. Compared to the palm edge, the forearm has a much thinner SC which only contains a few cell layers; therefore, depolarization is not observed in the DOPU image of the forearm. To validate that the yellow band is exactly the SC, histopathology will be required in future studies. In the fourth column, the mole can be observed as a relatively low intensity region in both the *en face* and B-scan intensity images. In the DOPU image, slightly lower DOPU value (more yellow pixels) is observed in the mole region than in the surrounding area. The higher depolarization in the mole region is likely caused by the higher concentration of melanin because melanosomes are considered as non-spherical particles.

#### 4. Discussions and conclusion

The polarization and depolarization properties of skin can be important biomarkers for skin cancer detection. However, depolarization of light in tissue is complex because there are multiple mechanisms that can depolarize light, such as scattering from non-spherical particles, surface roughness, and multiple scattering. PS-OCT has the potential to differentiate the different mechanisms based on its high resolution in 3D and high sensitivity to depolarization. First, depolarization caused by scattering from non-spherical particles is usually highly localized in tissue. For example, a yellow band (low DOPU value) is observed in the top-layer of epidermis in thick skin which is likely due to depolarization from flattened cells in the stratum corneum. Another example is the RPE layer in retinal imaging, where RPE shows significantly lower DOPU due to the scattering from melanosomes which are ellipsoid shaped [26]. Second, the surface roughness can affect the depolarization through reflection and refraction. The surface reflected signal is shown on the surface of the tissue in the DOPU image. Currently this part of the signal is not included in our DOPU analysis due to the glaring effect. The glaring effect caused by strong reflections may disturb the Jones matrices measured at the surface boundary. In the future, it may be possible to reliably analyze this part of the signal when index matching is applied to reduce surface glaring. On the other hand, refraction on the surface boundary affects all the backscattered photons coming from below the surface. We have proposed a mechanism how refraction affects the depolarization in Section 2.3. Basically, the spatial fluctuation of the rough surface increases the randomness and broadens the range of the scattering angle captured by the OCT system, which results in a lower DOPU. The change of DOPU due to refraction on rough surface affects all the pixels below the surface, and thus it can be regarded as a global or average change of DOPU over the entire tissue thickness. Third, depolarization due to multiple scattering is suspected to impact the photons that have been detected at deeper regions. Separating the single-scattered and multiple-scattered photons is a challenging question and more investigations are necessary in the future. Therefore, by analyzing the 3D DOPU image at different depths and regions, it is possible to differentiate the different mechanisms of depolarization. Furthermore, the multiple contrasts in PS-OCT such as the intensity contrast and birefringence contrast can further improve the characterization of the surface profile and layered tissue structures, providing additional information for understanding depolarization in tissue.

Currently, our approach controls the noise effect by setting a threshold of  $\text{SNR} > 13 \text{ dB}$  on the pixels where DOPU is computed. For future work, improving the algorithm of DOPU will be investigated to further reduce the effect of noise. Makita et. al. developed a de-noising algorithm (M-DOPU) which has been shown to be robust to noise and can improve DOPU image quality especially when the SNR is relatively low [45]. In the future, we can apply the M-DOPU algorithm for improving the quantification of depolarization in skin imaging.

For future work, we will apply PS-OCT imaging to characterize skin lesions. For characterizing skin lesions, the melanin concentration, surface roughness, and collagen organization may change their properties over time and location during the formation and progression of melanoma.

Melanoma contains a higher degree of skin pigmentation due to melanin and the skin surface becomes smoother as melanoma progresses. Using a mouse model, Ceolato et al. reported that melanoma evolved towards a glossy surface as the result of a decrease in surface roughness [19]. They have measured an increase in DOP in melanoma compared with healthy skin. A recent study has shown that the stiffness and alignment of the extracellular matrix of collagen have a close connection with the metastasis of tumor cells during the development of melanoma [46]. PS-OCT has multiple imaging contrasts that can provide a comprehensive characterization of melanoma. The intensity contrast can visualize the morphology of skin layers and especially the surface profile in 3D. The DOPU contrast can assess the depolarization in tissue, which is related to surface roughness and scattering from non-spherical particles such as melanosomes. Although not shown in this paper, our PS-OCT system can also acquire phase retardation image that can detect tissue birefringence [37,47]. Tissue birefringence is highly sensitive to collagen fiber organization and orientation, which is useful for characterizing collagen disruption during tumor growth. Therefore, by integrating the information from the multiple contrasts acquired simultaneously in a single 3D measurement, PS-OCT can be a potential clinical tool to study melanoma progression.

In summary, this study investigates PS-OCT imaging, especially the DOPU contrast, for characterizing the depolarization property of skin tissue. To investigate the impact of surface roughness on depolarization, skin phantoms with various surface roughness levels and optical properties mimicking skin are imaged and the DOPU values are quantified and compared. The result shows a correlation between DOPU contrast and surface roughness, where a higher roughness corresponds to a lower DOPU value. By applying an index matching, such effect is significantly reduced, which confirms the impact of surface condition on light depolarization. Through preliminary *in vivo* skin imaging, the capability of DOPU in detecting depolarization in skin is further demonstrated. By utilizing the 3D spatial information benefited from PS-OCT imaging, DOPU can offer a high-resolution depth differentiation as well as precise quantification of depolarization in tissue.

**Funding.** Natural Sciences and Engineering Research Council of Canada (CHRP 508405-17, RGPIN-2017-05913); Canadian Institutes of Health Research (CPG-151974).

**Disclosures.** The authors declare no conflicts of interest.

**Data availability.** Data underlying the results presented in this paper are not publicly available at this time but may be obtained from the authors upon reasonable request.

## References

1. Z. Apalla, D. Nashan, R. B. Weller, and X. Castellasqué, "Skin cancer: epidemiology, disease burden, pathophysiology, diagnosis, and therapeutic approaches," *Dermatol. Ther.* **7**(S1), 5–19 (2017).
2. C. M. Balch, J. E. Gershenwald, S. Soong, J. F. Thompson, M. B. Atkins, D. R. Byrd, A. C. Buzaid, A. J. Cochran, D. G. Coit, S. Ding, A. M. Eggermont, K. T. Flaherty, P. A. Gimotty, J. M. Kirkwood, K. M. McMasters, M. C. Mihm Jr, D. L. Morton, M. I. Ross, A. J. Sober, and V. K. Sondak, "Final version of 2009 AJCC melanoma staging and classification," *J. Clin. Oncol.* **27**(36), 6199–6206 (2009).
3. American Cancer Society, "Cancer Facts and Figures 2020," <https://www.cancer.org/content/dam/cancer-org/research/cancer-facts-and-statistics/annual-cancer-facts-and-figures/2020/cancer-facts-and-figures-2020.pdf>
4. L. Izikson, A. J. Sober, M. C. Mihm Jr., and A. Zembowicz, "Prevalence of melanoma clinically resembling seborrheic keratosis: analysis of 9204 cases," *Arch. Dermatol.* **138**(12), 1562–1566 (2002).
5. T. P. Jones, P. E. Boiko, and M. W. Piepkorn, "Skin biopsy indications in primary care practice: a population-based study," *J. Am. Board Fam. Med.* **9**(6), 397–404 (1996).
6. A. J. Sober, T. B. Fitzpatrick, M. C. Mihm Jr., T. G. Wise, B. J. Pearson, W. H. Clark, and A. W. Kopf, "Early recognition of cutaneous melanoma," *JAMA* **242**(25), 2795–2799 (1979).
7. P. J. Christos, S. A. Oliveria, M. Berwick, G. DuPont, D. E. Elder, M. Synnestvedt, J. A. Fine, R. L. Barnhill, and A. C. Halpern, "Signs and symptoms of melanoma in older populations," *J. Clin. Epidemiol.* **53**(10), 1044–1053 (2000).
8. K. Hashimoto, "New methods for surface ultrastructure: comparative studies of scanning electron microscopy, transmission electron microscopy and replica method," *Int. J. Dermatol.* **13**(6), 357–381 (1974).
9. M. C. L. Pacheco, M. F. P. C. Matins-Costa, A. J. P. Zapata, J. D. Cherit, and E. R. Gallegos, "Implementation and analysis of relief patterns of the surface of benign and malignant lesions of the skin by microtopography," *Phys. Med. Biol.* **50**(23), 5535–5543 (2005).

10. V. V. Tuchin, "Polarized light interaction with tissues," *J. Biomed. Opt.* **21**(7), 071114 (2016).
11. Y. Pan, D. S. Gareau, A. Scope, M. Rajadhyaksha, N. A. Mullani, and A. A. Marghoob, "Polarized and nonpolarized dermoscopy: the explanation for the observed differences," *Arch. Dermatol.* **144**(6), 828–829 (2008).
12. Z. Huang, H. Lui, X. K. Chen, A. Alajlan, D. I. McLean, and H. Zeng, "Raman spectroscopy of in vivo cutaneous melanin," *J. Biomed. Opt.* **9**(6), 1198–1206 (2004).
13. P. R. Bargo and N. Kollias, "Measurement of skin texture through polarization imaging," *Br. J. Dermatol.* **162**(4), 724–731 (2010).
14. Y. Sun, J. W. Su, W. Lo, S. J. Lin, S. H. Jee, and C. Y. Dong, "Multiphoton polarization imaging of the stratum corneum and the dermis in ex-vivo human skin," *Opt. Express* **11**(25), 3377–3384 (2003).
15. S. L. Jacques, J. C. Ramella-Roman, and K. Lee, "Imaging skin pathology with polarized light," *J. Biomed. Opt.* **7**(3), 329–341 (2002).
16. L. Tchvialeva, G. Dhadwal, H. Lui, S. Kalia, H. Zeng, D. I. McLean, and T. K. Lee, "Polarization speckle imaging as a potential technique for in vivo skin cancer detection," *J. Biomed. Opt.* **18**(6), 061211 (2012).
17. D. C. Louie, J. Phillips, L. Tchvialeva, S. Kalia, H. Lui, W. Wang, and T. K. Lee, "Degree of optical polarization as a tool for detecting melanoma: proof of principle," *J. Biomed. Opt.* **23**(12), 1 (2018).
18. P. Ghassemi, P. Lemaillet, T. A. Germer, J. W. Shupp, S. S. Venna, M. E. Boisvert, K. E. Flanagan, M. H. Jordan, and J. C. Ramella-Roman, "Out-of-plane Stokes imaging polarimeter for early skin cancer diagnosis," *J. Biomed. Opt.* **17**(7), 0760141 (2012).
19. R. Ceolato, M. Golzio, C. Riou, X. Orlik, and N. Riviere, "Spectral degree of linear polarization of light from healthy skin and melanoma," *Opt. Express* **23**(10), 13605–13612 (2015).
20. B. Baumann, S. O. Baumann, T. Konegger, M. Pircher, E. Götzinger, F. Schlanitz, C. Schütze, H. Sattmann, M. Litschauer, U. Schmidt-Erfurth, and C. K. Hitzenberger, "Polarization sensitive optical coherence tomography of melanin provides intrinsic contrast based on depolarization," *Biomed. Opt. Express* **3**(7), 1670–1683 (2012).
21. D. Huang, E. A. Swanson, C. P. Lin, J. S. Schuman, W. G. Stinson, W. Chang, M. R. Hee, T. Flotte, K. Gregory, C. A. Puliafito, and J. G. Fujimoto, "Optical coherence tomography," *Science* **254**(5035), 1178–1181 (1991).
22. J. Welzel, E. Lankenau, R. Birngruber, and R. Engelhardt, "Optical coherence tomography of the human skin," *J. Am. Acad. Dermatol.* **37**(6), 958–963 (1997).
23. S. Askaruly, Y. Ahn, H. Kim, A. Vavilin, S. Ban, P. U. Kim, S. Kim, H. Lee, and W. Jung, "Quantitative evaluation of skin surface roughness using optical coherence tomography in vivo," *IEEE J. Sel. Top. Quantum Electron.* **25**(1), 1–8 (2019).
24. M. Ulrich, T. Braunmühl, H. Kurzen, T. Dirschka, C. Kellner, E. Sattler, C. Berking, J. Welzel, and U. Reinhold, "The sensitivity and specificity of optical coherence tomography for the assisted diagnosis of nonpigmented basal cell carcinoma: an observational study," *Br. J. Dermatol.* **173**(2), 428–435 (2015).
25. A. Rajabi-Estarabadi, J. M. Bittar, C. Zheng, V. Nascimento, I. Camacho, L. G. Feun, M. Nasiriavanaki, M. Kunz, and K. Nouri, "Optical coherence tomography imaging of melanoma skin cancer," *Lasers Med. Sci.* **34**(2), 411–420 (2019).
26. E. Götzinger, M. Pircher, B. Baumann, C. Ahlers, W. Geitzenauer, U. Schmidt-Erfurth, and C. K. Hitzenberger, "Three-dimensional polarization sensitive OCT imaging and interactive display of the human retina," *Opt. Express* **17**(5), 4151–4165 (2009).
27. B. Baumann, J. Schirmer, S. Rauscher, S. Fialová, M. Glösmann, M. Augustin, M. Pircher, M. Gröger, and C. K. Hitzenberger, "Melanin pigmentation in rat eyes: in vivo imaging by polarization-sensitive optical coherence tomography and comparison to histology," *Invest. Ophthalmol. Visual Sci.* **56**(12), 7462–7472 (2015).
28. C. E. Saxer, J. F. de Boer, B. H. Park, Y. Zhao, Z. Chen, and J. S. Nelson, "High-speed fiber-based polarization-sensitive optical coherence tomography of in vivo human skin," *Opt. Lett.* **25**(18), 1355–1357 (2000).
29. Y. Yasuno, S. Makita, Y. Sutoh, M. Itoh, and T. Yatagai, "Birefringence imaging of human skin by polarization-sensitive spectral interferometric optical coherence tomography," *Opt. Lett.* **27**(20), 1803–1805 (2002).
30. M. Pircher, E. Goetzinger, R. Leitgeb, and C. K. Hitzenberger, "Three dimensional polarization sensitive OCT of human skin in vivo," *Opt. Express* **12**(14), 3236–3244 (2004).
31. E. Li, S. Makita, Y. J. Hong, D. Kasaragod, and Y. Yasuno, "Three-dimensional multi-contrast imaging of in vivo human skin by Jones matrix optical coherence tomography," *Biomed. Opt. Express* **8**(3), 1290–1305 (2017).
32. M. Bonesi, H. Sattmann, T. Torzicky, S. Zotter, B. Baumann, M. Pircher, E. Götzinger, C. Eigenwillig, W. Wieser, R. Huber, and C. K. Hitzenberger, "High-speed polarization sensitive optical coherence tomography scan engine based on Fourier domain mode locked laser," *Biomed. Opt. Express* **3**(11), 2987–3000 (2012).
33. J. Strasswimmer, M. C. Pierce, B. H. Park, V. Neel, and J. F. de Boer, "Polarization-sensitive optical coherence tomography of invasive basal cell carcinoma," *J. Biomed. Opt.* **9**(2), 292–299 (2004).
34. L. Duan, T. Marvdashti, A. Lee, J. Y. Tang, and A. K. Ellerbee, "Automated identification of basal cell carcinoma by polarization-sensitive optical coherence tomography," *Biomed. Opt. Express* **5**(10), 3717–3729 (2014).
35. T. Marvdashti, L. Duan, S. Z. Aasi, J. Y. Tang, and A. K. E. Bowden, "Classification of basal cell carcinoma in human skin using machine learning and quantitative features captured by polarization sensitive optical coherence tomography," *Biomed. Opt. Express* **7**(9), 3721–3735 (2016).
36. D. Y. Diao, L. Tchvialeva, G. Dhadwal, H. Lui, D. I. McLean, and T. K. Lee, "Durable rough skin phantom for optical modelling," *Phys. Med. Biol.* **59**(2), 485–492 (2014).

37. X. Zhou, M. J. Ju, L. Huang, and S. Tang, "Slope-based segmentation of articular cartilage using polarization-sensitive optical coherence tomography phase retardation image," *J. Biomed. Opt.* **24**(03), 1–14 (2019).
38. M. I. Mishchenko and J. W. Hovenier, "Depolarization of light backscattered by randomly oriented nonspherical particles," *Opt. Lett.* **20**(12), 1356–1358 (1995).
39. E. Bahar and M. A. Fitzwater, "Depolarization and backscatter enhancement in light scattering from random rough surfaces: comparison of full-wave theory with experiment," *J. Opt. Soc. Am. A* **6**(1), 33–43 (1989).
40. M. Zerrad, J. Sorrentini, G. Soriano, and C. Amra, "Gradual loss of polarization in light scattered from rough surfaces: electromagnetic prediction," *Opt. Express* **18**(15), 15832–15843 (2010).
41. X. Zhou, D. C. Louie, S. Maloufi, L. Huang, Q. Liu, L. Tchvialeva, T. K. Lee, and S. Tang, "Polarization sensitive optical coherence tomography for assessing skin roughness," *Proc. SPIE* **11211**, 112110A (2020).
42. S. G. Adie, T. R. Hillman, and D. D. Sampson, "Detection of multiple scattering in optical coherence tomography using the spatial distribution of Stokes vectors," *Opt. Express* **15**(26), 18033–18049 (2007).
43. M. Huzaira, F. Rius, M. Rajadhyaksha, R. R. Anderson, and S. González, "Topographic variations in normal skin, as viewed by in vivo reflectance confocal microscopy," *J. Invest. Dermatol.* **116**(6), 846–852 (2001).
44. C. Griffiths, J. Barker, T.O. Bleiker, R. Chalmers, and D. Creamer, eds., *Rook's Textbook of Dermatology* (John Wiley & Sons, 2008).
45. S. Makita, Y. J. Hong, M. Miura, and Y. Yasuno, "Degree of polarization uniformity with high noise immunity using polarization-sensitive optical coherence tomography," *Opt. Lett.* **39**(24), 6783–6786 (2014).
46. A. Kaur, B. L. Ecker, S. M. Douglass, C. H. Kugel III, M. R. Webster, F. V. Almeida, R. Somasundaram, J. Hayden, E. Ban, H. Ahmadzadeh, J. Franco-Barraza, N. Shah, I. A. Mellis, F. Keeney, A. Kossenkov, H. Tang, X. Yin, Q. Liu, X. Xu, M. Fane, P. Brafford, M. Herlyn, D. W. Speicher, J. A. Wargo, M. T. Tetzlaff, L. E. Haydu, A. Raj, V. Shenoy, E. Cukierman, and A. T. Weeraratna, "Remodeling of the collagen matrix in aging skin promotes melanoma metastasis and affects immune cell motility," *Cancer Discov.* **9**(1), 64–81 (2019).
47. X. Zhou, F. Eltit, X. Yang, S. Maloufi, H. Alousaimi, Q. Liu, L. Huang, R. Wang, and S. Tang, "Detecting human articular cartilage degeneration in its early stage with polarization-sensitive optical coherence tomography," *Biomed. Opt. Express* **11**(5), 2745–2760 (2020).